RESEARCH OUTPUTS / RÉSULTATS DE RECHERCHE

The role of thioredoxin reductase in gold nanoparticle radiosensitization effects

Penninckx, Sébastien; Heuskin, Anne-Catherine; Michiels, Carine; Lucas, Stéphane

Link to publication

Nanomedicine

The role of thioredoxin reductase in gold nanoparticle radiosensitization effects

Sébastien Penninckx*,1, Anne-Catherine Heuskin1, Carine Michiels2 & Stéphane Lucas1
1Research Center for the Physics of Matter & Radiation (PMR-LARN), Namur Research Institute for Life Sciences (NARILIS),
University of Namur, Rue de Bruxelles, 61, B-5000 Namur, Belgium
2Unité de Recherche en Biologie Cellulaire (URBC), Namur Research Institute for Life Sciences (NARILIS), University of Namur, Rue
de Bruxelles 61, B-5000 Namur, Belgium
*Author for correspondence: sebastien.penninckx@unamur.be

Aim: To identify new mechanisms responsible for the radiosensitization effect of gold nanoparticles (GNPs). **Materials & methods:** A549 lung carcinoma cells were incubated with 10-nm GNPs during 6 or 24 h before to be exposed to 25 keV/μm protons or 225 kV x-rays. **Results:** GNP incubation led to a time-dependent mitochondria membrane depolarization, oxidative stress and to x-ray and proton radiosensitization. Moreover, a marked inhibition of thioredoxin reductase was observed. Irradiation of cells invalidated for thioredoxin reductase evidenced a radiosensitization effect, suggesting that this enzyme is a potential GNP target. **Conclusion:** We suggest that GNPs play a radiosensitizer role by weakening detoxification systems. Altogether, these results open up promising novel strategies for the development of nanotechnologies associated to radiotherapy.

Over the last decade, radiotherapy has been the main treatment modality used against cancer [1]. Although a great deal of effort has been devoted to this matter, radiotherapy is still limited by side effects caused to healthy tissues surrounding the tumor. One of the current challenges is to find new approaches that would maximize the differential response between the radiation dose deposited in the tumor and in normal healthy tissues (the so-called 'therapeutic ratio'). In this way, the research on optimized treatment modalities, such as intensity-modulated radiation therapy and hadrontherapy, is growing worldwide. Hadrontherapy is an emerging radiation treatment that uses charged particles like protons (as suggested by Wilson in 1946 [2]) instead of conventional x-ray photons. The major advantage of using these charged particles is a better spatial distribution of the absorbed dose. Indeed, the maximum energy deposition occurs at an adjustable selected depth (Bragg peak) and the beam can be scanned laterally to conform with the tumor 3D volume [3]. These unique properties ensure a more effective tumor targeting.

In the meantime, the development of nanomedicine offers the possibility to take advantage of nanoscale materials for diagnosis and therapeutic applications [4–7], including radiotherapy. In the pioneering work of Hainfeld *et al.*, injections of 1.9-nm gold nanoparticles (GNPs) showed an increase in the survival of tumor-bearing mice in combination with 250 kVp x-rays compared with x-rays alone [8]. Up to now, many *in vitro* [9–14] and *in vivo* studies [8,12–15] have evidenced the ability of high-atomic number nanoparticles, injected into the tumor, to amplify the x-ray radiation treatment efficiency. The potential use of these nano-objects enables to decrease the radiation dose, thereby reducing the risk to damage normal tissues. GNPs have been extensively studied due to their high absorption coefficient, good biocompatibility [16] and their ability to improve the performance of MRI diagnosis [17]. Their radiosensitization effect has been demonstrated for a variety of different cell lines [18] including colon [19,20], breast [21,22], prostate [23–25], brain [14,21,26] and bladder [9] cancer cell lines using radiation ranging from kV [23,24,26] to 9 MV [20] x-ray and charged particles [9,10,27]. Preclinical studies have reported that large GNP sizes (typically above 50 nm) could be trapped by the reticuloendothelial system leading to lower tumor uptake and accumulation in the liver and spleen [28,29]. To cope with this limitation, small size gold nanoclusters (GNCs) have been designed

Future Medicine

to escape reticuloendothelial system absorption and the renal clearance barrier [15,30,31]. Indeed, Zhang *et al.* [15] demonstrated that intraperitoneal injection of sub-2-nm GNCs in mice enables a high selective tumor uptake. Moreover, they reported a strong radiosensitization effect after γ-ray irradiation even though the tumor uptake was at the ppm level, which is extremely low compared with *in vivo* GNP experiments [32].

Despite strong interest in these investigations, the mechanism(s) responsible for the radiosensitization effect of GNPs remains poorly understood, yet a mandatory step toward the clinical use of gold radiosensitizers. The present work aims at shedding light on mechanisms responsible for the radiosensitization effect of GNPs in combination with protons and x-rays. In this work, we focused on the effect of homemade 10-nm amino-PEG-functionalized GNPs on human lung carcinoma A549 cells. We evidenced cellular dysfunctions caused by the GNP internalization, suggesting a biological mechanism associated to the radiosensitization effect. The rationalization of these cellular dysfunctions enabled to identify a new potential biological target of GNPs: the thioredoxin reductase (TrxR) enzyme.

Materials & methods
Cell culture
Human lung carcinoma A549 cells were grown in Eagle's Minimum Essential Medium (MEM Glutamax; Gibco® by Life Technologies, MA, USA) supplemented with 10% (v/v) fetal bovine serum (FBS; Gibco by Life Technologies, MA, USA) at 37°C in a humidified atmosphere incubator containing 5% CO_2.

GNP synthesis & characterization
The 10 nm amine-PEG-functionalized GNPs were synthesized via a method described in [33]. Briefly, $HAuCl_4$ (Sigma–Aldrich, Overijse, Belgium) and TA-PEG$_{550}$-OCH$_3$ (Biochempeg Scientific, Inc., MA, USA) were mixed at a 2000:1 Au:PEG molar ratio in deionized water and stirred at room temperature for 1 h. NABH$_4$ (Sigma–Aldrich) was then added to the mixture under vigorous stirring and the solution was left stirring during 3 h. Then, TA-PEG$_{400}$-NH$_2$ (Biochempeg Scientific, Inc.) and NABH$_4$ were added to the solution for extra passivation. After 3 h of stirring, the colloidal suspension was purified with a membrane filtration device (Vivaspin, Millipore, Belgium).

GNPs were lyophilized with a freeze-drying system (Alpha 2–4 LD Plus; Analis, Belgium) and stored at 4°C for further use as in [10]. Prior to incubation with cells, the lyophilized GNPs were resuspended in cell medium and sonicated for 15 min. In all the experiments of this study, the cells were incubated with 50 μg of gold per ml of medium, which corresponds to 8.22 nM of GNPs. The transmission electron microscopy (TEM) study was performed with an FEI Tecnai 10 instrument (100 kV). A drop of the sample was deposited on a holey carbon film-coated copper grid (Formvar/Carbon 200 mesh, Copper, TED Pella, CA, USA).

GNP localization using confocal microscopy
50,000 cells were seeded in 24-well plates containing coverslips (13-mm cover glasses; VWR, Belgium). After a 24-h incubation at 37°C, the medium was replaced for MEM supplemented with 10% FBS and 50 μg Au.ml^{-1} GNPs. Cells incubated without GNPs were used as a control. After a 24 h incubation, the cells were fixed for 10 min with 4% paraformaldehyde (Merck Chemicals, Belgium) and washed with phosphate-buffered saline (PBS) three-times. The nuclei and F-actin were stained with Hoechst 33258 (Molecular Probes™ by Life Technologies) and Alexa Fluor® 555 Phalloidin (Molecular Probes by Life Technologies), respectively. Cells were then washed three-times with PBS. After that, the coverslips were mounted in Mowiol (Sigma–Aldrich) and observed with a Leica SP5 confocal-inverted microscope. The fluorescence signal of dyes associated to the nuclei and F-actin were detected using, respectively, a 405-nm UV laser and a 561-nm laser. Additionally, a 514-nm laser was used to detect the presence of GNPs, using surface plasmon resonance as described in [34]. Optical stacks of 0.5 μm were taken through the cells in order to accurately localize the GNPs in the cytoplasm.

GNP internalization
5×10^4 cells were seeded as 50 μl drops in 24-well plates, in order to mimic the irradiation condition before to be placed in an incubator at 37°C with 5% CO_2. 2 h after seeding, the wells were filled with MEM + 10% FBS and placed in the incubator overnight. The medium was then removed, the wells were filled with MEM + 10% FBS without (control cells) or with 50 μg Au.ml^{-1} of GNPs and incubated at 37°C. After a given incubation time, the cells were detached using 0.25% trypsin. They were pelleted by centrifugation (1000 rpm, 5 min, 4°C) and the

media were discarded. The pellet was resuspended in 500 μl of PBS and side-scattered (SSC) light was analyzed immediately using a FACS Calibur flow Cytometer (BD Biosciences, NJ, USA). 20,000 cells were analyzed per sample using Cell Quest Pro Software (BD Biosciences).

Gold content quantification was performed by atomic absorption spectroscopy. After a 24-h incubation with GNPs, the cells were washed twice with PBS at 37°C and then trypsinized. Detached cells were then washed twice with culture medium by successive centrifugation. The actual number of cells in each sample was then determined using a cell counter (Countess Automated Cell Counter, Invitrogen, CA, USA). After the third centrifugation, the medium was discarded, and the pellets were digested using 2 ml of aqua regia (37% HCl, 65% HNO_3 Sigma–Aldrich) overnight. The samples' gold content was quantified using an atomic absorption spectrophotometer (AA-7000F from Shimadzu, Japan) by plotting the calibration curve with known concentrations of a gold standard solution (Merck Chemicals, Belgium) used for external calibration. Triplicate readings were analyzed for each sample. The amount of gold detected in the cells was expressed as an internalized gold quantity (pg) per cell.

Proton beam irradiation

The detailed protocols can be found in [35]. Briefly, 48 h before irradiation, 5×10^4 cells were seeded as 32-μl drops at the center of sterilized homemade irradiation chambers, closed with a plastic cap to avoid dehydration and infection and placed in an incubator at 37°C with 5% CO_2. 2 h after seeding, MEM was added and the chambers were placed in the incubator overnight. The medium was then removed, the wells were filled with MEM + 10% FBS without (control cells) or with 50 μg Au.ml^{-1} of GNPs and incubated at 37°C until irradiation (6 or 24 h in our experiments). Prior to irradiation, the medium was discarded from the irradiation chamber, the plastic cap was removed and a sterile cotton swab was used to take away the cells, which might have diffused outside the irradiated field. The chamber was then closed again with the plastic cap, rinsed with PBS and filled with a CO_2-independent medium (Gibco by Life Technologies). The cell monolayer was irradiated with a homogenous proton beam over 1 cm^2, produced by a 2-MV Tandem accelerator (High Voltage Engineering Europa). The reader is referred to [36] for a thorough description of the experimental setup and irradiation procedure. Briefly, the energy of the beam was tuned in order to deliver the desired LET within the cells to be irradiated. Pristine proton peaks were extracted in air through a 1-μm silicon nitride window and the irradiation chambers were placed on a sample holder fixed at the end of the beamline. Homogeneity was achieved by defocusing the beam and checked with a passivated implanted planar silicon detector moved along the x and y directions. The dose rate was assessed every millimeter in a 1 cm^2 surface and errors were less than 5% in the cell sample region. The LET at the cell sample location was computed with a SRIM software. In this study, a 25 keV μm^{-1} LET value (beam energy: 1.3 MeV) was chosen to obtain the maximum relative biological effectiveness for a proton beam. The dose rate was fixed to 3 Gy.min^{-1} and the dose range was chosen to cover the survival fraction down to a few percent. All doses were calculated using the classic broad beam formula:

$$D = \frac{1.6\,10^{-9}\ \text{LET}\ \Phi}{\rho}$$

Here, the density ρ is taken as 1 g/cm^3 and Φ is the proton beam fluence. All the experiments were repeated in triplicate on separate days. All curve fittings were performed with the OriginLab® software (MA, USA). A linear-quadratic equation was used to fit clonogenic assay data:

$$SF = e^{-(\alpha D + \beta D^2)}$$

Where SF is the surviving fraction of the cells; α and β define the linear and the quadratic components, respectively, and D is the deposited dose.

x-ray irradiation

48 h before irradiation, 50,000 cells were seeded as 50 μl drops in 24-well plates and placed in an incubator at 37°C with 5% CO_2. 2 h after seeding, the wells were filled with MEM supplemented with 10% FBS and placed in the incubator overnight. The medium was then removed, the wells were filled with MEM + 10% FBS without (control cells) or with 50 μg Au.ml^{-1} of GNPs and incubated at 37°C until irradiation (6 or 24 h in our

experiments). Prior to irradiation, the medium was discarded from the wells, the plate was rinsed with PBS and filled with CO_2-independent medium (Gibco by Life Technologies). The cell monolayer was irradiated with a homogenous x-ray beam produced by a X-Rad 225 XL (PXi Precision x-ray, CT, USA) at 225 kV. The dose rate was fixed to 3 Gy.min^{-1} and the dose range was chosen to cover the survival fraction down to a few percent.

Clonogenic assay

Immediately after irradiation, the cells were detached using 0.25% trypsin and they were counted. In order to obtain countable colony numbers for different radiation doses, the cells were seeded in 6-well plates containing MEM supplemented with 10% FBS, penicillin/streptomycin and incubated at 37°C. In parallel, cells were also seeded in separate dishes at one density per dose. 2 h after seeding, they were fixed with 4% paraformaldehyde (Merck Chemicals, Belgium) for 10 min and washed with PBS three-times. The cells attached to the dish were counted manually under an optical microscope to obtain the precise number of cells seeded for each cell density and dose. 11 days postirradiation, the colonies were stained with violet crystal in 2% ethanol. The amount of visible colonies (containing 50 or more cells) was considered to represent the surviving cells, which were counted manually. The plating efficiency (PE) was determined for each irradiation dose and calculated by dividing the amount of colonies by the initial numbers of seeded cells. The surviving fraction was obtained as the PE ratio for irradiated cells to the PE for control cells. The control cells underwent every procedure except the irradiation step. At least three independent experiments were performed and the errors were evaluated as standard deviation (SD). In order to quantify the GNPs ability to enhance cell death, we calculated two indicators, the amplification factor (AF) and the sensitization enhancement ratio (SER), from the fitted surviving curves:

$$AF[\%] = \left[\frac{SF_{control}^{fitted\ curve} - SF_{GNPs}^{fitted\ curve}}{SF_{control}^{fitted\ curve}} \right] \times 100$$

$$SER = \frac{Radiation\ dose\ without\ GNPs}{Radiation\ dose\ with\ GNPs}$$

The AF indicates the enhanced proportion of dead cells in the presence of GNPs compared with irradiation alone for a given dose. On the other hand, the SER is calculated for a given biological effect, usually a 10% survival fraction.

DNA damage study

50,000 cells were seeded in 24-well plates containing coverslips (13 mm cover glasses; VWR, Belgium). After a 24 h incubation at 37°C, the medium was replaced for MEM supplemented with 10% FBS and 50 μg Au.ml^{-1} of GNPs. Cells incubated without GNPs were used as control. After a 6 h incubation, the cells were irradiated. After different incubation time after irradiation, cells were fixed for 10 min with 4% paraformaldehyde (Merck Chemicals) and washed with PBS three-times. The nuclei were stained with To-pro (Molecular Probes by Life Technologies). 53BP1 foci were labeled using an anti-53BP1 antibody coupled to Alexa Fluor 488 (Santa Cruz Biotechnology; sc-515841, TX, USA). The cells were then washed with PBS three-times. After that, the coverslips were mounted in Mowiol (Sigma–Aldrich) and observed with a Leica SP5 confocal-inverted microscope. In order to analyze the kinetics of the DNA repair process, we introduced a mathematical model based on the one described in [37]. Readers can refer to Supplementary information (S1) for further details on the mathematical model.

Mitochondrial membrane & oxidative stress measurement

5×10^4 cells were seeded as 50 μl drops in 24-well plates in order to mimic the irradiation condition before to be placed in an incubator at 37°C with 5% CO_2. 2 h after seeding, the wells were filled with MEM + 10% FBS and placed in the incubator overnight. The medium was then removed, the wells were filled with MEM + 10% FBS without (control cells) or with 50 μg Au.ml^{-1} of GNPs and incubated at 37°C. After a given incubation time, the cells were detached using 0.25% trypsin. They were pelleted by centrifugation (1000 rpm, 5 min, 4°C) and the medium was discarded. The pellet was resuspended and incubated during 20 min at 37°C in 500 μl of 100 nM

tetramethylrhodamine ethyl ester perchlorate (Sigma–Aldrich) in MEM or in 10 μM 5-(6)-chloromethyl-2′-7′-dichlorodihydro-fluorescein diacetate (ThermoFisher, MA, USA) in HBSS (Gibco by Life Technologies, MA, USA) for, respectively, mitochondrial membrane potential and oxidative stress measurement. The cells were then pelleted by centrifugation (1000 rpm, 5 min, 4°C) and the medium was discarded. The pellet was resuspended in 500 μl of PBS and the fluorescence was analyzed immediately with a FACS Calibur flow Cytometer (BD Biosciences). 20,000 cells were analyzed per sample. The Cell Quest Pro Software (BD Biosciences, NJ, USA) was used to analyze the data.

Cell proliferation measurement

An MTS assay was used to measure the proliferation rate. 2×10^3 cells were seeded as 50 μl drops in 96-well plates and placed in an incubator at 37°C with 5% CO_2. 2 h after seeding, the wells were filled with MEM + 10% FBS and placed in the incubator overnight. The medium was then removed, the wells were filled with MEM + 10% FBS without (control cells) or with 50 μg Au.ml^{-1} of GNPs and incubated at 37°C. After a given incubation time, the medium was discarded, the wells were rinsed with PBS and 120 μl of MEM + 10% FBS medium containing MTS (Cell Titer 96® Aqueous One Solution Reagent; Promega, WI, USA) in a 6:1 ratio was added in each well. After a 1-h incubation with an MTS tetrazolium compound, the optical density at 490 nm was determined using a spectrophotometer (X-Mark™ Microplate Spectrophotometer; Biorad, CA, USA).

TrxR activity assay

The TrxR activity was measured with a commercially available kit (Sigma–Aldrich). The kit is based on the catalytic reduction of 5,5′-dithiobis(2-nitrobenzoic) acid to 5-thio-2-nitrobenzoic acid by TrxR. This reduction generates a strong yellow colored product. Its absorbance is measurable by spectrophotometry. The cells were incubated 24 h with or without 50 μg Au.ml^{-1} of GNPs before to being detached with 0.25% trypsin. The cells were pelleted by centrifugation (1000 rpm, 5 min, 4°C) and the medium was discarded. The pellet was resuspended in a homemade lysis buffer (9% w/w sucrose; 5% v/v aprotinin [Sigma–Aldrich], in deionized water) and disrupted by a dounce homogenizer. Then, the TrxR activity was measured according to the manufacturer's instructions. The linear increase in absorbance at 412 nm was measured during 10 min using a spectrophotometer (Ultrospec 8000; GE Healthcare, IL, USA). The TrxR activity rate was calculated from the slope of absorbance at 412 nm versus time.

siRNA transfection

A549 cells were seeded at 50,000 cells/well in a 24-well plate and left 24 h in an incubator at 37°C with 5% CO_2. The day after, the cells were transfected with 50-nM human TrxR siRNA (On-target plus Human TXNRD1 – Smart pool, Dharmacon, CO, USA) using a Dharmafect 1 (Dharmacon, CO, USA) transfection reagent according to the manufacturer's instructions. In the meantime, Risc-free siRNA (Dharmacon, CO, USA) was used as a negative control. The transfection medium was replaced after 24 h by fresh MEM culture medium supplemented with 10% FBS. The cells were then incubated for 24 h before irradiation.

Western blotting

A549 cells were scrapped in a Laemmli lysis buffer (1 M Tris-HCl pH 6.8, 10% SDS, 20% glycerol). The protein content per sample was evaluated using a nanodrop (Nanodrop 1000, ThermoScientific). The proteins were separated by electrophoresis on a 10% SDS-PAGE gel using a migration buffer (25 mM Tris-HCl, 192 mM glycin, 3.5 mM SDS) and then transferred onto a nitrocellulose membrane (Nitrocellulose membranes 0.2 μm; BioRad, CA, USA). The membrane was blocked 1 h at room temperature in an Odyssey blocking buffer (BD Biosciences, MJ, USA) in PBS 50/50 v/v before an overnight incubation at 4°C in an Odyssey blocking buffer with 0.1% Tween containing a specific antibody: a mouse anti-TrxR monoclonal antibody (SC-28321; Santa Cruz Biotechnology, TX, USA) or a mouse anti-β-actin monoclonal antibody (A-5441; Sigma–Aldrich). After three washes of 5 min in PBS-0.1% Tween, a 1-h incubation with a goat antimouse IR Dye-labeled secondary antibody (Licor) was performed in an Odyssey blocking buffer with 0.1% Tween at room temperature. After three extra washes of 5 min in PBS-0.1% Tween and two washes in PBS, the membrane was dried at 37°C and scanned using an Odyssey infrared imaging system (Licor). Immunodetection of β-actin was used as loading control.
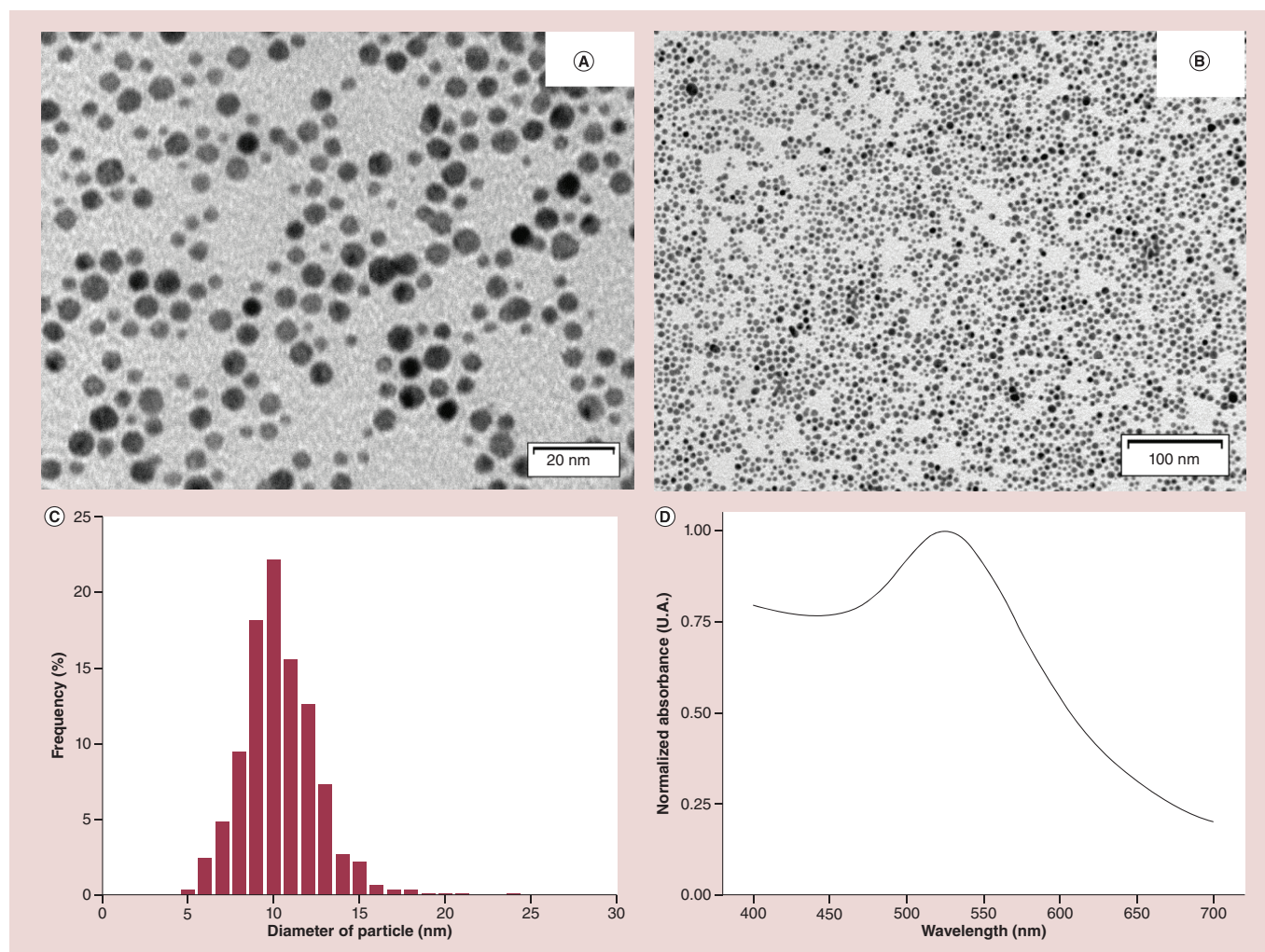
Figure 1.   Characterization of amino-PEG functionalized gold nanoparticles. (A & B) Morphological images of gold nanoparticles obtained by transmission electron microscopy, scale bar: 20 **(A)** or 100 nm **(B)**. **(C)** Size distribution histogram obtained by the analysis of 1000 particles on five transmission electron microscopy images taken at different magnifications. The mean diameter is 10.11 ± 0.06 nm. **(D)** UV–Vis absorption spectrum of gold nanoparticles evidencing a maximum absorption peak at 525 nm.

Statistical analysis

All experiments were repeated at least three-times on separate days. Results were reported as mean $\pm$ corresponding SD. In addition, a one-way analysis of variance (ANOVA) was performed using Origin 8 in order to compare the differences between groups. The number of asterisks in the figures indicates the level of statistical significance as follows: * $p < 0.05$, **$p < 0.01$, ***$p < 0.001$.

Results

GNP synthesis & characterization

The amino-PEG functionalized GNPs used in this study were prepared through a revisited Turkevich method, previously described in [33]. A ligand TA-PEG$_{400}$-NH$_2$ was chosen as the coating in order to increase the colloidal stability and prevent aggregation. The TEM images (Figure 1A & B) showed that the synthesized GNPs were spherical in shape and well-dispersed. An average diameter of 10.11 ± 0.06 nm was measured by analysis of 1000 particles on five TEM images taken at different magnifications (Figure 1C). Moreover, the UV–vis absorption spectrum (Figure 1D) showed a peak centered at 525 nm, corresponding to the plasmon resonance band of nanoparticles.

Cell internalization study

Preliminary cytotoxicity investigations of GNPs on A549 cells have shown no significant toxicity on a concentration range until 100 $\mu g.ml^{-1}$ (Supplementary Figure 2). In the frame of this work, we established that an incubation of 50 μg $Au.ml^{-1}$ of GNPs in the medium during 24 h did not generate any cytotoxicity and therefore allows internalization and irradiation experiments.

GNPs need to be internalized by cells in order to exert a potential radiosensitization effect. Hence, the intracellular localization of GNPs and their spatial distribution were investigated by confocal microscopy. This technique was used to detect both the scattered light of label-free GNPs and the fluorescence of molecular dyes used for labeling cell components. The control cells (Figure 2A) exhibited only blue and red areas corresponding, respectively, to the signal of Hoechst dye from the nucleus and Alexa Fluor Phalloidin 555 from the cytoplasm. No GNPs were observed in the control cells. The cells incubated in the presence of GNPs during 3 and 24 h exhibited some green spots in addition to the fluorescence signals from nucleus and cytoplasm (Figure 2B & C). Each of these green spots is the fingerprint of the scattered light from a GNP cluster. After a 3 h incubation (Figure 2B), GNP aggregates were mainly distributed in the close vicinity of the plasma membrane. After a 24 h incubation, GNP aggregates were localized in the cytoplasm close to the nucleus. It is notable that GNPs seem to self-agglomerate in bigger aggregates and move from the plasma membrane surface to the perinuclear region over time. In order to investigate whether GNPs were internalized into the cells or attached on the cell surface, scattered light and fluorescence images were taken at different depths, from the bottom to the top, inside one cell volume. The Z-stacks of Figure 2D show the entrapment of GNPs into red area (i.e., into the cytoplasm), confirming the internalization of GNPs into A549 cells.

In order to study the kinetic of GNP internalization, SSC light in flow cytometry was used to follow the nanoparticle uptake. As described by Toduka *et al.* [38], when nano-objects are taken up into cells, they increase the intracellular density changing the SSC intensity. As shown in Figure 2E, a quick cell uptake of GNPs was observed during the first 6 h of incubation. Afterward, a plateau was observed. One-way ANOVA analysis showed no significant difference upon longer incubation times, in other words, between 6 and 24 h of incubation ($p < 0.05$). The measured data points were fitted to one-phase exponential association curve, according to the formula:

$$Y = Y_{max}[1 - \exp(-k.\,t)]$$

Where Y is the SSC intensity (proportional to the uptake level), Y_{max} is the maximal uptake level, k is the first-order rate constant in per hours and t is the incubation time of GNPs in hours. The first-order constant was determined from the fitted curve as 0.52 ± 0.04 h^{-1}. These flow cytometry results are in agreement with the confocal fluorescence microscopy analyses (Figure 2) showing a larger GNP internalization after 24 h compared with a 3-h incubation.

Finally, the actual amount of GNPs internalized by A549 cells was determined by atomic absorption spectroscopy and reached 2.0 ± 0.4 pg of gold per cell after a 24-h incubation corresponding to 1.9×10^5 GNPs per cell.

Cellular impact of GNPs

In order to probe the cellular impact of GNPs, A549 cells were incubated with GNPs during varying incubation times (ranging from 0 to 24 h). At each defined incubation time, two cellular processes were investigated: oxidative stress and mitochondria homeostasis. As shown in Figure 3A and B, a significant decrease in mitochondrial membrane potential ($\Delta\psi m$) and an increase in the reactive oxygen species (ROS) level were observed during the first 6 h of incubation in the presence of GNPs. At this time point, minimal $\Delta\psi m$ ($77 \pm 2\%$ of control fluorescence) and the maximal ROS level (1.4 ± 0.1-fold change) were observed. After this incubation time, a slow recovery leading to mitochondria membrane repolarization and reduction of the oxidative stress were detected until a 24-h GNP incubation. The kinetic process observed for $\Delta\psi m$ was confirmed by ATP content measurements, which showed the same behavior according to the GNP incubation time (Supplementary Figure 3). It is interesting to note that the maximal cellular dysfunctions were measured when cell uptake reached a plateau (Figure 2E). In parallel, we observed the initiation of autophagy, which was markedly increased after a 12- and 18-h incubation but no longer after a 24 h incubation (Supplementary Figure 4). We hypothesized that the autophagy could be responsible for the elimination of dysfunctional mitochondria, hence for the cell recovery.
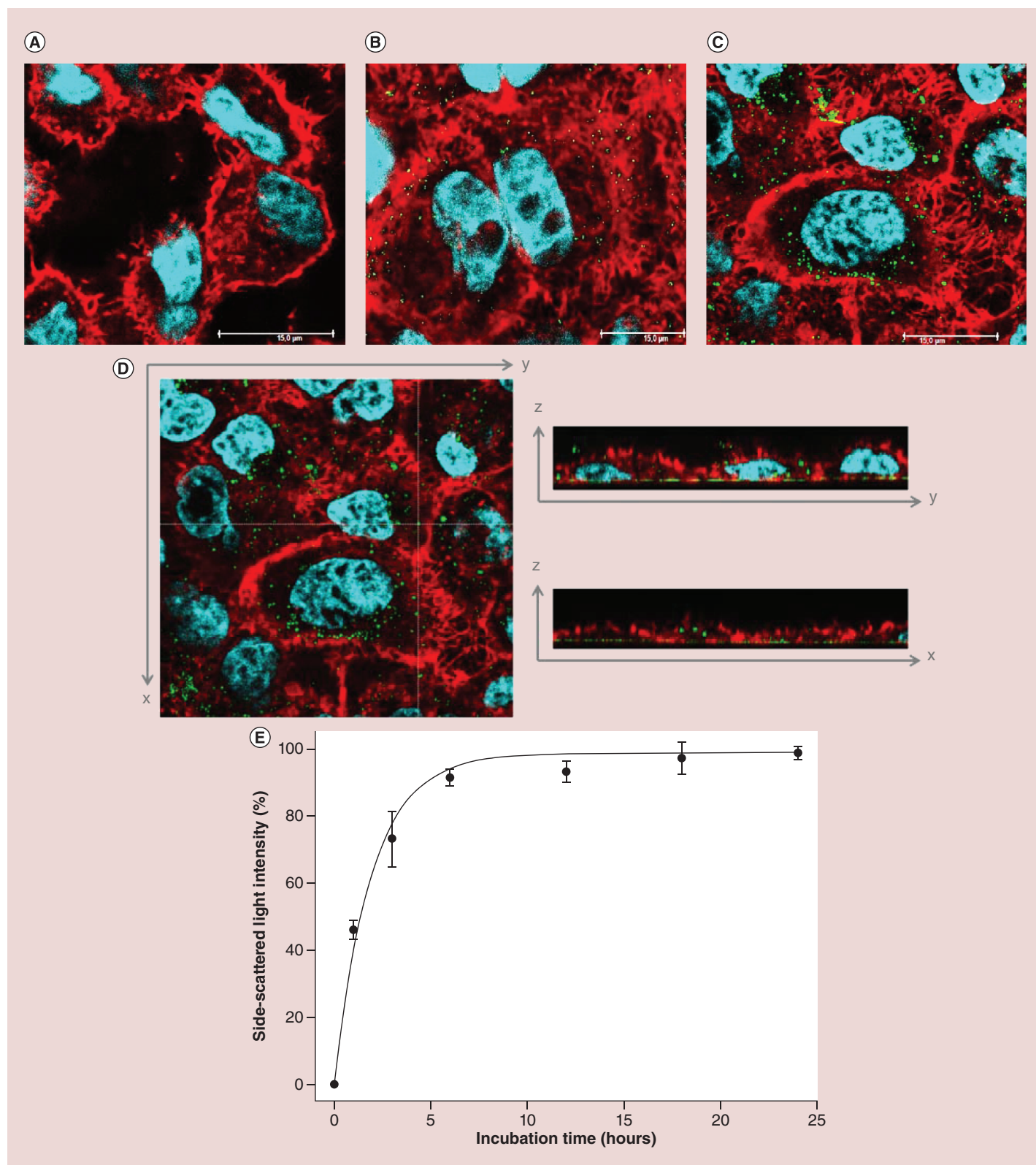
Figure 2.   Gold nanoparticle uptake in A549 cells. Confocal microscopy images of gold nanoparticle intracellular localization **(A)** control cells free of GNPs; **(B)** cells preincubated with 50 μg Au.ml^{-1} of gold nanoparticles during 3 h; **(C)** cells preincubated with 50 μg Au.ml^{-1} of GNPs during 24 h, scale bar: 15 μm. **(D)** The Z profiles of cells (transversal view) were obtained after 24 h of incubation with 50 μg Au.ml^{-1} of gold nanoparticles. Blue and red areas, respectively, represent the signal of Hoechst from the nucleus and Alexa Fluor® Phalloidin 555 from the cytoplasm. Green areas represent the localization of the gold nanoparticle clusters. The white dashed lines indicate the axes studied in the Z-profile images. **(E)** Kinetics of gold nanoparticle uptake for a concentration of 50-μg Au.ml^{-1} of gold nanoparticles using flow cytometry. The curve is plotted as mean values relative to untreated control (sample after a 0 h incubation) $\pm$ standard deviation of three independent experiments and nonlinear regression curve according to a one-phase exponential association curve.
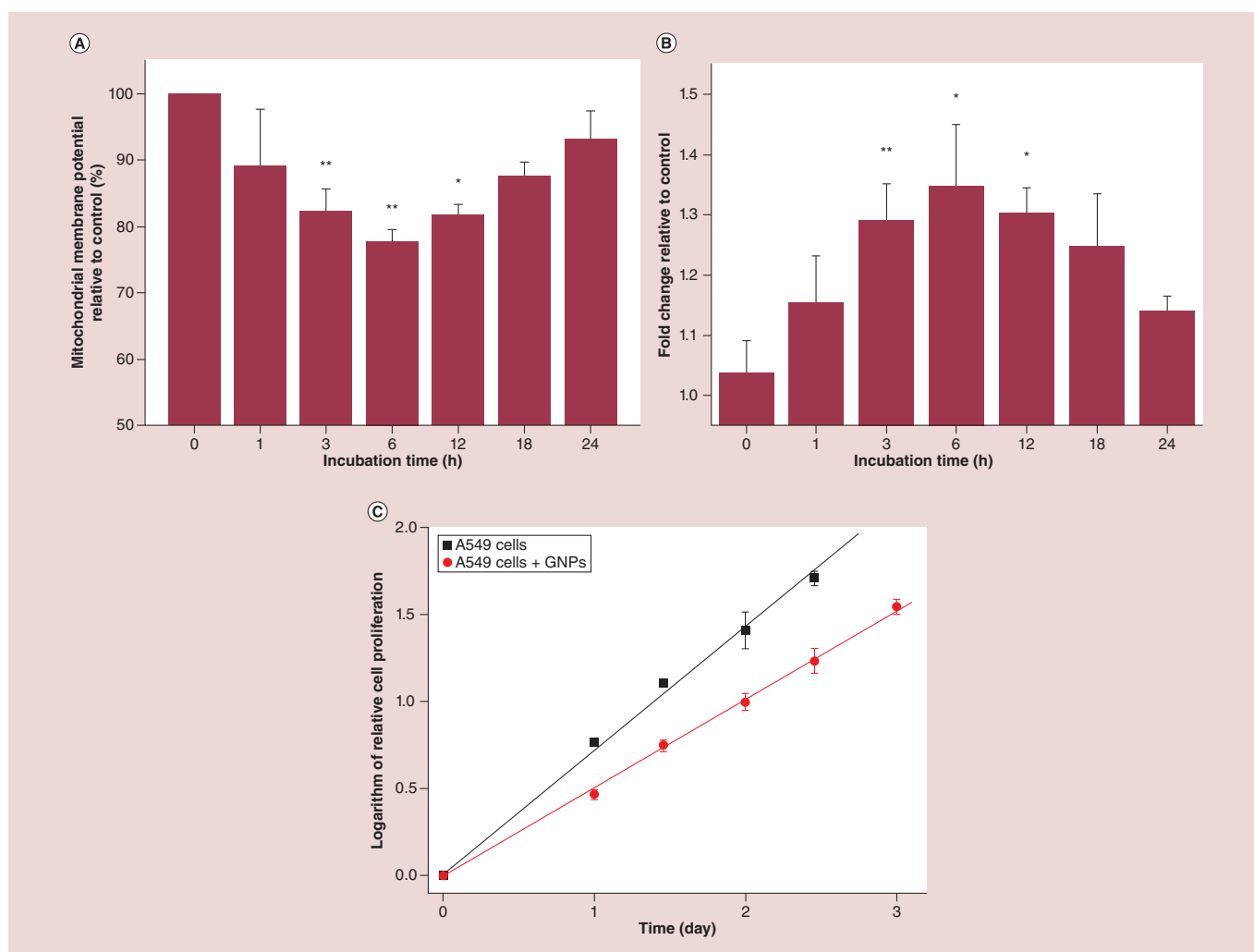
Figure 3. Gold nanoparticles cause dysfunctions in biological pathways. (A) Mitochondrial membrane potential assessed using TMRE fluorescent dye over incubation time in the presence of 50 μg Au.ml^{-1} of GNPs. **(B)** Reactive oxygen species levels measured using the CM-H2DCFDA fluorescent dye over incubation time in the presence of 50 μg Au.ml^{-1} of GNPs. TMRE **(A)** and CM-H2DCFDA **(B)** intensities are reported relative to the untreated control cells intensity (A549 cells without GNPs) for each given time post-incubation. **(C)** Cell proliferation of A549 cells pre-incubated during 24 h in the presence or not of 50 μg Au.ml^{-1} of GNPs. All data are plotted as mean values ± SD of at least three independent replicates. Results were statistically analyzed using a one-way ANOVA (Tukey test, *p < 0.05, **p < 0.01).
ANOVA: Analysis of variance; CM-H2DCFDA: 5-(6)-chloromethyl-2′,7′-dichlorodihydro-fluorescein diacetate; GNP: Gold nanoparticle; SD: Standard deviation; TMRE: Tetramethylrhodamine ethyl ester perchlorate.

An MTS assay was used in order to investigate the influence of GNPs on cell proliferation. It revealed that following a 24-h incubation, GNPs significantly reduced the cell proliferation rate (Figure 3C). Doubling times of 32.9 h ± 0.3 and 23.2 h ± 0.4 were measured in A549 cells incubated, respectively, in the presence and in the absence of GNPs.

Cell death enhancement by GNPs upon irradiation

A549 cells pre-incubated during 24 h with or without GNPs were irradiated using protons or x-rays. The cell survival was quantified by standard clonogenic assays. Dose–response curves are presented in Figure 4A. In both cases, the survival fraction exponentially decreased with increasing radiation dose. Moreover, this decrease was more pronounced when cells were pre-incubated with GNPs, evidencing a radiosensitization effect of GNPs. The cell survival (surviving fraction) curves were fitted with the linear quadratic model and the α and β values determined by the fitting procedure are reported in Table 1. Results indicated that the presence of GNPs in A549 cells induced
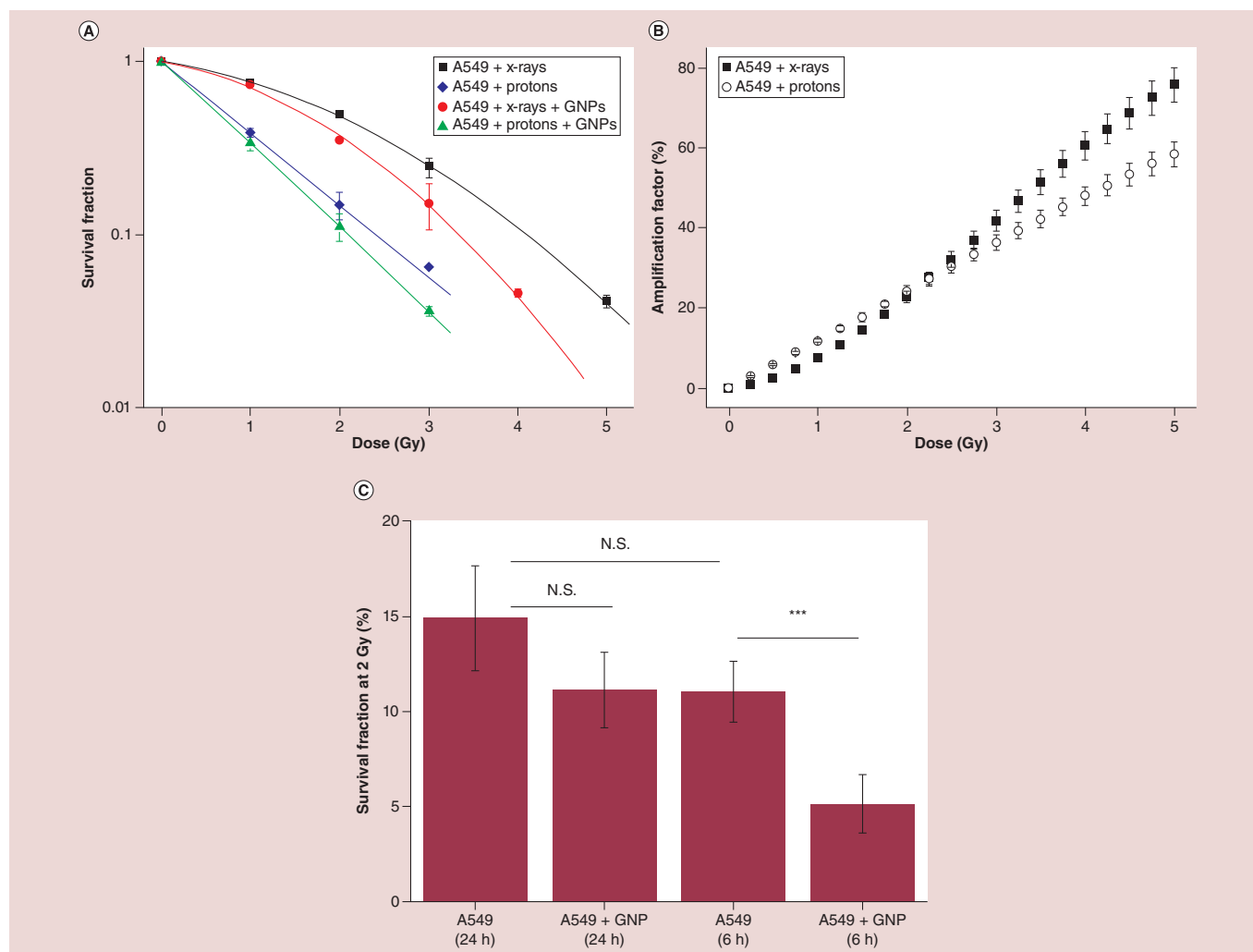
Figure 4.   Irradiation experiments. (A) Survival curve of A549 cells incubated during 24 h in MEM without GNPs and irradiated by x-rays (■, black curve); without GNPs and irradiated by protons (♦, blue curve); with 50 μg Au.ml^{-1} of GNPs and irradiated by x-rays (●, red curve); with 50 μg Au.ml^{-1} of GNPs and irradiated by protons (▲, green curve). Results are expressed as mean values ± SD of at least three independent experiments. **(B)** Amplification factors obtained from fits of survival fraction curves after 25 keV/μm proton beam (○) or 225 kV x-rays (■). **(C)** Survival fraction of A549 cells incubated during 6 and 24 h with or without GNPs and exposed to 2 Gy of protons. Results are expressed as mean values ± SD of three independent experiments. Results were statistically analyzed using a one-way ANOVA (Tukey test, N.S.: Not significant, *** $p < 0.01$).
ANOVA: Analysis of variance; GNP: Gold nanoparticle; MEM: Eagle's minimum essential medium; SD: Standard deviation.

Table 1. Calculated α, β coefficients and sensitization enhancement ratio at 10% survival for A549 cells irradiated by a 25 keV/μm proton beam or 225 kV x-rays after being pre-incubated during 24 h with 50 μg Au.ml^{-1} of GNPs as well as in untreated control cells (without GNPs). The α, β values are also reported for TrxR-invalidated A549.

Beam	Sample	α (Gy^{-1})	β (Gy^{-2})	SER 10%
Protons	A549	0.96 ± 0.03	–	1.14
	A549 + GNPs	1.071 ± 0.003	–	
x-ray	A549	0.18 ± 0.02	0.092 ± 0.006	1.22
	A549 + GNPs	0.21 ± 0.04	0.14 ± 0.01	
x-ray	A549 + siRF	0.22 ± 0.03	0.09 ± 0.01	1.24
	A549 + siTrxR	0.30 ± 0.06	0.13 ± 0.02	

GNP: Gold nanoparticle; RF: Risc-free; SER: Sensitization enhancement ratio; TrxR: Thioredoxin reductase.
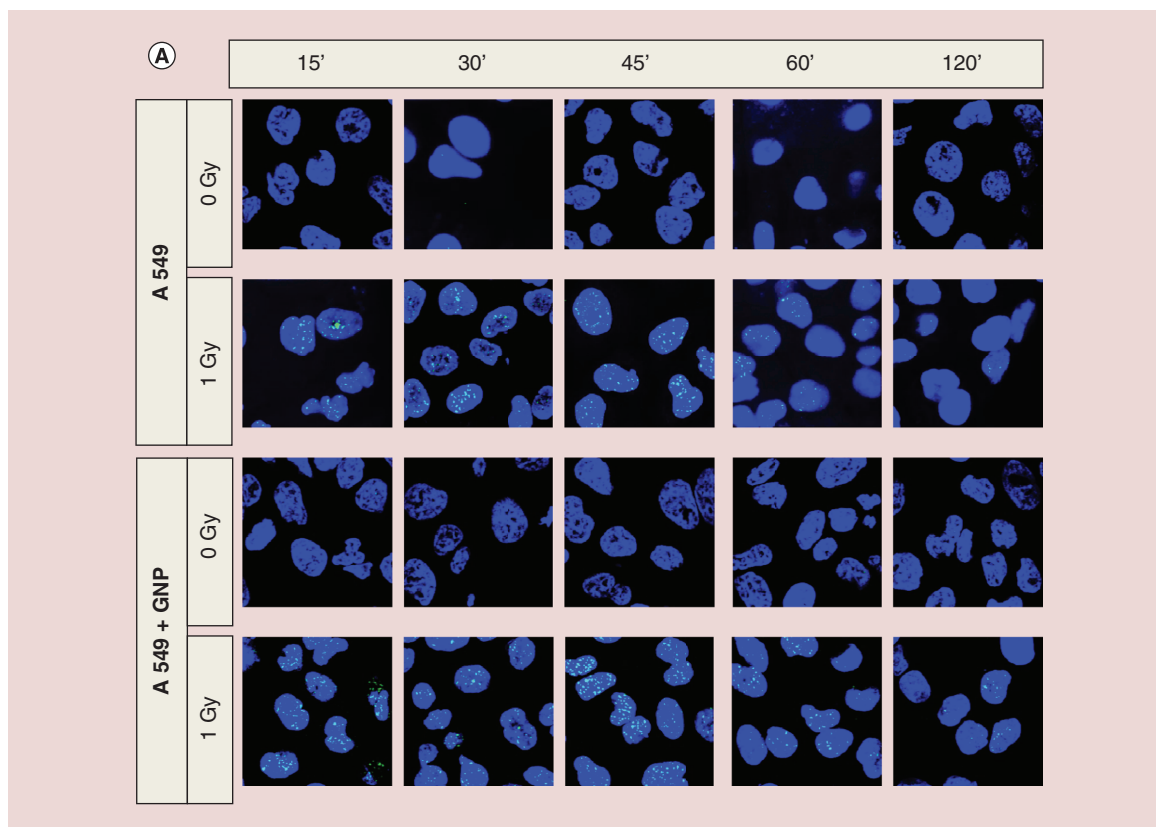
Figure 5.   DNA damage study after irradiation. (A) Representative immunofluorescence labeling of 53BP1 for A549 cells pre-incubated with or without 50 µg Au.ml⁻¹ GNPs. Cells were exposed to 1 Gy x-ray and fixed at different times after irradiation (0, 15, 30, 45, 60, 120, 240 min). Blue and green areas represent the signal of To-pro dye from the nucleus and 53BP1 labeling, respectively. **(B)** Quantification of the number of 53BP1 RIF in A549 without GNPs at different times after exposition. Results are plotted as mean values ± SD. Quantification was performed on a minimum of 150 cells per condition; n = 3. **(C)** Quantification of the number of 53BP1 RIF in A549 cells containing GNPs at different times after exposition. Results are plotted as mean values ± SD. Quantification was performed on a minimum of 150 cells per condition; n = 3.
GNP: Gold nanoparticle; RIF: Radiation-induced foci; SD: Standard deviation.

a $16 \pm 3\%$ and $11.6 \pm 0.2\%$ increase in the α parameter after, respectively, x-rays and proton irradiation as well as a $52 \pm 4\%$ increase in the β parameter in case of x-rays.

The AF indicates the enhanced proportion of dead cells in the presence of GNPs compared with irradiation alone for a given dose [10]. This indicator was plotted as a function of the irradiation dose for both types of radiation (Figure 4B). This graph shows that the AF increased with the irradiation dose. At 2 Gy, a clinically relevant dose per fraction delivered to patients, a $22 \pm 1\%$ and $24 \pm 1\%$ AF was calculated from, respectively, x-rays and protons. No significant difference in the AF was reported for x-rays compared with proton irradiation at 2 Gy. Interestingly, Figure 4C shows a more pronounced radiosensitization effect, when A549 were pre-incubated with GNPs during 6 h ($AF_{2Gy} = 54\%$) compared with 24 h ($AF_{2Gy} = 24\%$). SER at 10% survival were calculated as 1.14 and 1.22 for proton and x-ray irradiation, respectively. These results demonstrate that GNPs can produce a significant increase in the cell death induced by radiation that is modulated according to the duration of the incubation time.

DNA damage repair after irradiation

In order to further examine the influence of GNPs when cells were irradiated, the level of 53BP1, a DNA double-strand break (DSBs) sensing protein [37,39] was evaluated by immunofluorescence labeling. Quantification of radiation-induced foci over post-irradiation time showed a similar profile for A549 cells pre-incubated in the presence (Figure 5C) or in the absence of GNPs (Figure 5B). Indeed, 53BP1 radiation-induced foci appeared during the first 15 min post-irradiation (1 Gy x-ray). Then, their number decreased with time. To analyze the kinetics of
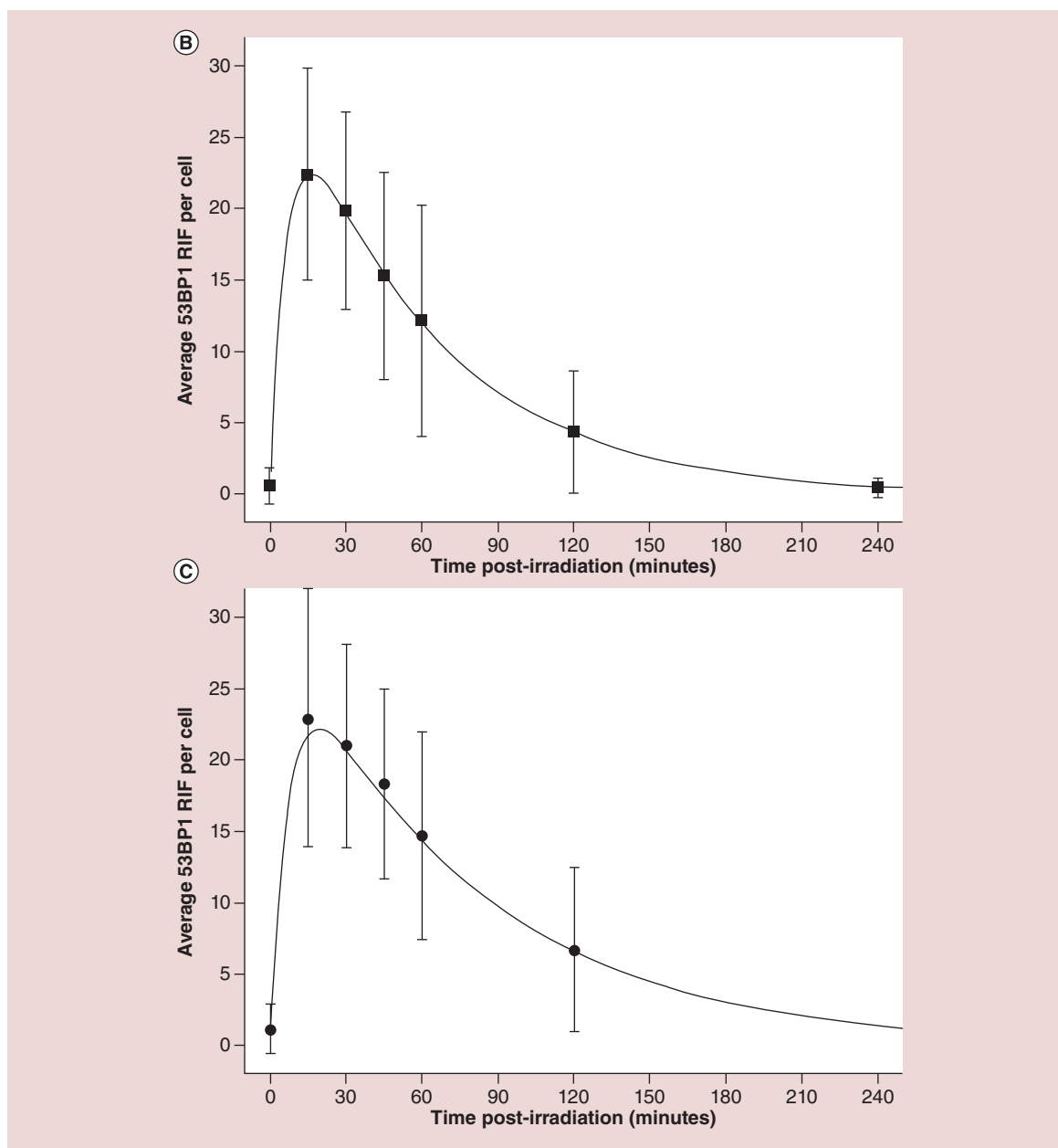
Figure 5.   DNA damage study after irradiation (cont.). (A) Representative immunofluorescence labeling of 53BP1 for A549 cells pre-incubated with or without 50 μg Au.ml⁻¹ GNPs. Cells were exposed to 1 Gy x-ray and fixed at different times after irradiation (0, 15, 30, 45, 60, 120, 240 min). Blue and green areas represent the signal of To-pro dye from the nucleus and 53BP1 labeling, respectively. **(B)** Quantification of the number of 53BP1 RIF in A549 without GNPs at different times after exposition. Results are plotted as mean values ± SD. Quantification was performed on a minimum of 150 cells per condition; n = 3. **(C)** Quantification of the number of 53BP1 RIF in A549 cells containing GNPs at different times after exposition. Results are plotted as mean values ± SD. Quantification was performed on a minimum of 150 cells per condition; n = 3.
GNP: Gold nanoparticle; RIF: Radiation-induced foci; SD: Standard deviation.

this DNA damage repair process, experimental data were fitted using Equation 1 (see Supplementary data Equation 1) and coefficient values determined by the fitting procedure are reported in Table 2. Results indicated that the presence of GNPs in A549 cells did not influence the total number of DSBs per cell (29.4 ± 0.6 DSBs/Gy compared with 28.3 ± 0.6 DSBs/Gy for cells incubated without and with GNPs, respectively) but led to a 25% decrease in the repair process rate (k_2 coefficient).

Table 2. Fitted coefficients for A549 cells exposed to 1 Gy of 225 kV x-rays after pre-incubation during 6 h with or without 50 μg Au.ml⁻¹ of gold nanoparticles.					
Sample	A (DSBs/Gy)	B (RIF)	k_1 (min⁻¹)	k_2 (min⁻¹)	R^2
A549	29.4 ± 0.6	0.51	0.146 ± 0.007	0.0172 ± 0.0004	0.9996
A549 + GNPs	28.3 ± 0.6	1.11	0.14 ± 0.01	0.0129 ± 0.0005	0.9990

A and B represent the total number of radiation-induced foci created per Gy of radiation and the number of radiation-induced foci detected in unirradiated control cells, respectively. k1 and k2 are kinetic parameters that reflect the time it takes to detect one DSB and the time it takes to repair the DSBs. R2 is the coefficient of determination from the fitting procedure. DSB: Double-strand break; GNP: Gold nanoparticle; RIF: Radiation-induced foci.

Role of TrxR in the radiosensitization effect

In this study, TrxR was identified as a potential GNP target. The activity of this enzyme was assessed in A549 cells incubated with or without GNPs during 24 h. As shown in Figure 6A & B, a $71 \pm 2\%$ decrease in the TrxR activity was observed when cells were pre-incubated with GNPs. To distinguish whether GNPs were responsible for an enzymatic inhibition or whether they downregulated the protein expression, the amount of TrxR protein was evaluated in A549 cells after incubation with and without GNPs. As shown in Figure 6C, no significant change in the TrxR protein level was reported in these conditions.

To confirm that TrxR inhibition may lead to a radiosensitization effect, invalidation of the TrxR expression was performed using siRNA. It led to a significant decrease in the mRNA level and a residual 15% TrxR protein level, which was confirmed by an activity assay (Supplementary Figure 5). Invalidated A549 cells were irradiated without GNPs in the same aforementioned conditions, evidencing a significant radiosensitization of TrxR invalidation (Figure 6D). The α and β values were determined and are reported in Table 1. Results evidenced that cells harboring a decreased functional TrxR level underwent an increase in the β parameter upon x-ray exposure.

Discussion

Given the emerging need to improve current treatment modalities against cancer, this *in vitro* study was undertaken to investigate the impact of the combination of GNPs and proton therapy on human cancer A549 cells. The kinetics analyses of the cell uptake process showed a quick internalization of GNPs during the first 6 h of incubation followed by a plateau from a 6 to 24 h incubation. This observation was also reported by Chithrani's group where the plateau was reached at 4–7 h, depending on the particle size [40]. Moreover, these authors evidenced a size-dependent uptake half-life, with smaller GNPs taken up faster ($T_{\frac{1}{2}}$ = 2.1 h for their 14-nm GNPs), which is in agreement with the uptake half-life calculated from our results ($T_{\frac{1}{2}}$ = 1.3 h). This curve form suggests that the GNPs enter into cells via a receptor-mediated endocytosis mechanism due to a nonspecific adsorption of serum proteins at the nanoparticle surface. This hypothesis is supported by the presence of some protein-characteristic bands in the UV/visible spectrum of GNPs incubated in a serum-containing media [40]. On the other hand, Hühn *et al.* [41] showed differences in the internalization efficiency when incubating human umbilical vein endothelial cells with nanoparticles in a serum-free and serum-containing media. Moreover, TEM images of cells pre-incubated with GNPs evidenced the clustering of nano-objects in vesicles that could be endosomes [10].

Our work highlighted a clear radiosensitization effect with 225 kV x-ray photons and 25 keV/μm protons enabling to eradicate about 25% more cells at 2 Gy compared with irradiation without GNPs. More interestingly, the proportion of extra dead cells reached $76 \pm 4\%$ when cells containing GNPs were exposed to 5 Gy x-ray photons. This result opens the door to clinical applications, especially in hypofractionation treatments or in stereotactic external-beam radiation therapy where high-radiation doses are used [42,43]. A limited number of works have investigated the radiosensitization effect with protons and showed contradictory results. Jeynes *et al.* showed no significant enhancement effect when RT112 cells containing 50-nm GNPs were irradiated using a 3-MeV proton beam [9]. On the other hand, by exposing DU145 cells pre-incubated with 40-nm GNPs to a clinical 160-MeV proton beam, Polf *et al.* observed a 15% enhancement in the relative biological effectiveness [25]. Furthermore, our group reported a LET-dependent radiosensitization effect when A431 cells containing 10-nm GNPs were irradiated using a 25-keV/μm proton beam [10]. In this study, the authors reported a 10% SER of 1.14 as well as in the present study.

In spite of the growing amount of data regarding GNPs-induced radiosensitivity, the responsible mechanisms remain poorly understood. In recent years, evidences for a physicochemical mechanism are growing. The difference in energy absorption between gold and the surrounding soft tissues enables a dose enhancement in cells containing GNPs. The interaction between the ionizing particles and high Z atoms leads to the emission of low-energy electrons
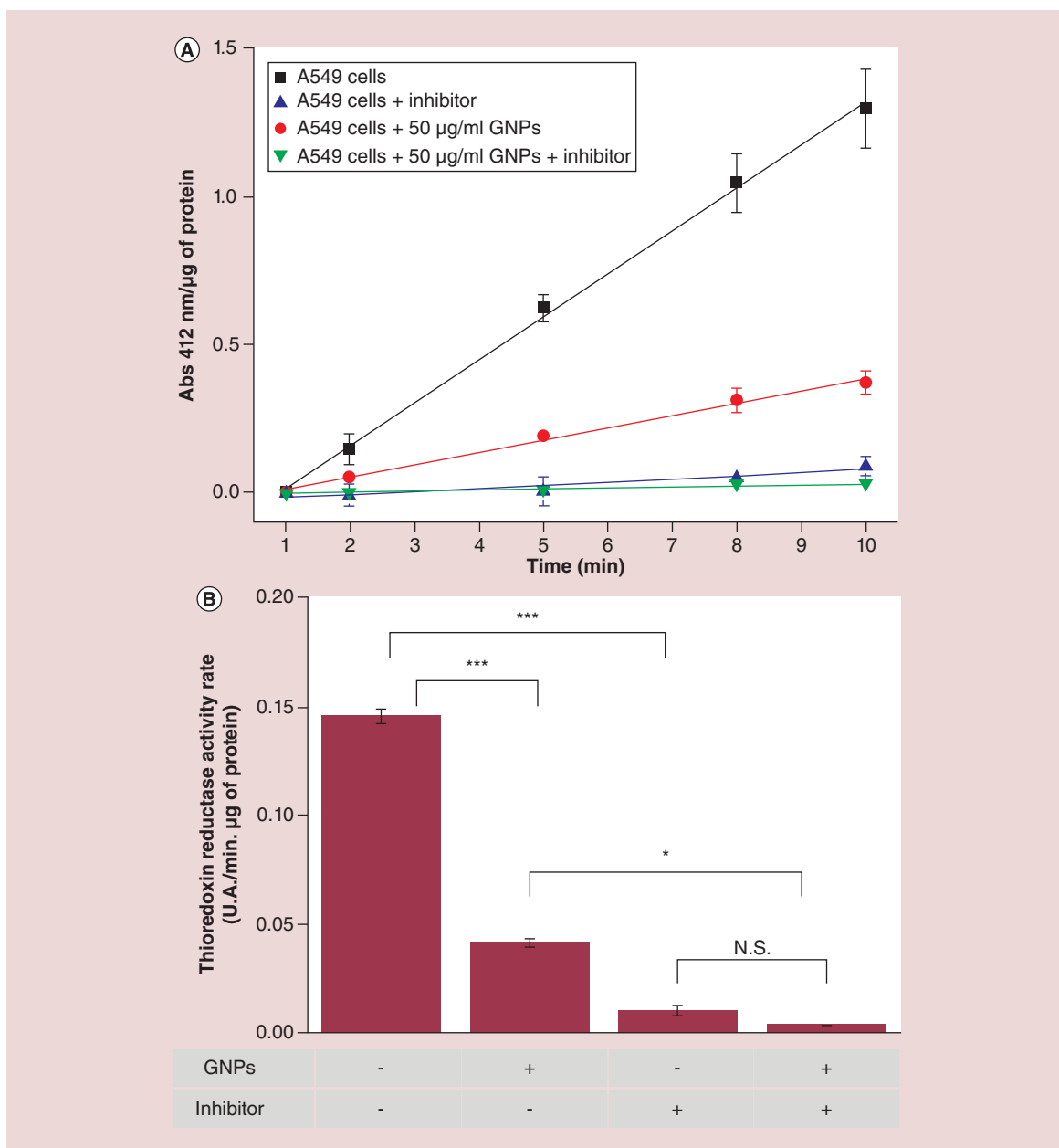
Figure 6.   TrxR as a potential target of GNPs. (A) TrxR activity measurement in A549 cells pre-incubated with or without 50 µg Au.ml^{-1} GNPs during 24 h. The activity is measured by the absorption at 412 nm over time. Data are plotted as mean values of absorbance normalized by the total protein content ± SD of three independent experiments. **(B)** TrxR activity rate calculated from the slope of TrxR activity curves. Data are plotted as mean values ± SD of three independent experiments. **(C)** The abundance of TrxR in A549 cells pre-incubated with or without 50 µg Au.ml^{-1} GNPs during 24 h was detected by western blotting. β-actin was used as loading control. TrxR fluorescence intensity was quantified and normalized for β-actin. **(D)** Survival curve of invalidated A549 cells using siRF as control (■, black curve) and siTrxR (●, red curve) after 225 kV x-ray irradiation. Results are expressed as mean values ± SD of three independent experiments. All results were statistically analyzed using a one-way ANOVA (Tukey test, *p < 0.05, ***p < 0.001, N.S.: Not significant).

ANOVA: Analysis of variance; GNP: Gold nanoparticle; N.S.: Not significant; RF: Risc-free; TrxR: Thioredoxin reductase; SD: Standard deviation.

Figure 6.   TrxR as a potential target of GNPs (cont.). (A) TrxR activity measurement in A549 cells pre-incubated with or without 50 μg Au.ml⁻¹ GNPs during 24 h. The activity is measured by the absorption at 412 nm over time. Data are plotted as mean values of absorbance normalized by the total protein content ± SD of three independent experiments. **(B)** TrxR activity rate calculated from the slope of TrxR activity curves. Data are plotted as mean values ± SD of three independent experiments. **(C)** The abundance of TrxR in A549 cells pre-incubated with or without 50 μg Au.ml⁻¹ GNPs during 24 h was detected by western blotting. β-actin was used as loading control. TrxR fluorescence intensity was quantified and normalized for β-actin. **(D)** Survival curve of invalidated A549 cells using siRF as control (■, black curve) and siTrxR (●, red curve) after 225 kV x-ray irradiation. Results are expressed as mean values ± SD of three independent experiments. All results were statistically analyzed using a one-way ANOVA (Tukey test, *p < 0.05, ***p < 0.001, N.S.: Not significant).
ANOVA: Analysis of variance; GNP: Gold nanoparticle; N.S.: Not significant; RF: Risc-free; TrxR: Thioredoxin reductase; SD: Standard deviation.
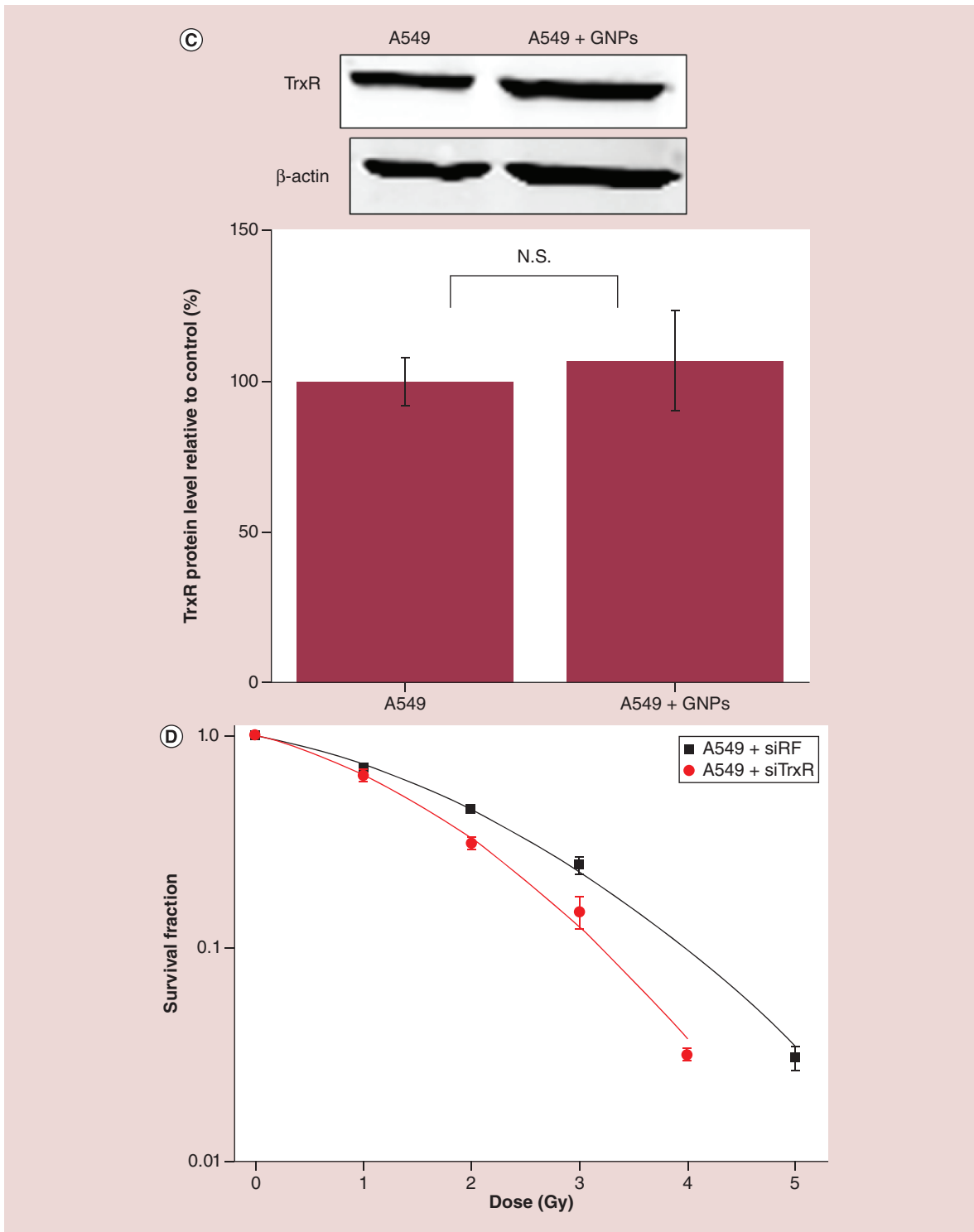
from the nanoparticle [44,45]. These electrons with an energy in the order of 100 eV interact with the surrounding medium, producing ROS. Several researchers have evidenced the production of these ROS in irradiated water solutions containing GNPs [46–48]. Misawa and Takahashi showed an increase in the production rate of hydroxyl radicals (1.46-fold) and superoxide anions (7.68-fold) in GNP solutions exposed to 100 kVp x-rays [46]. However, it seems unlikely that this mechanistic hypothesis can, on its own, explain the enhancement effect observed because it suffers from the need of a direct interaction between the incident beam and the nanoparticle. Indeed, Heuskin *et al.* recently demonstrated that the interaction probability of GNPs with the incident beam is very low when charged particles are considered [49]. Based on [10], they calculated a 10^{-6}–10^{-5} fraction of the total nanoparticle content actually interacting per Gy of radiation. Moreover, their simulations showed no increase in neither the macroscopic nor the microscopic dose in cells. In the meantime, Sotiropoulos *et al.* [50] reached the same conclusions and suggested that other mechanisms have greater contribution than physical interaction to the radiosensitization effect. For the first time, the present study evidences a GNP incubation time-dependent radiosensitization effect. Indeed, the AF at 2 Gy was 54% after a 6 h GNP incubation compared with 24% after 24 h. This drop in GNP-induced radiosensitvity over time is not in agreement with the aforementioned physical mechanism because cell uptake measurements demonstrated no significant change in the gold content between a 6 and 24 h incubation.

All these works open the door to new mechanistic hypotheses such as a potential biochemical mechanism. This study clearly evidenced that GNPs exert significant impacts on various important biological pathways. Several groups have evidenced that exposure to nanoparticles results in the production of ROS, which is one of the main cytotoxicity mechanisms [21,23,51,52]. Moreover, oxidative stress is known to cause mitochondria dysfunction through a depolarization of the mitochondrial membrane potential [53]. Our study showed a 25% mitochondrial membrane potential depolarization leading to a significant decrease in the ATP content after 6 h of GNP incubation. These results are in agreement with the results of Prise's group who reported a cell-dependent mitochondrial oxidation after GNP incubation [21]. Moreover, surface-enhanced Raman scattering measurement of 13-nm GNPs preincubated with A549 cells revealed that GNPs are in contact with biomolecules, which can be originating from mitochondria [54]. Although this result suggests a direct physical interaction with the mitochondria, additional investigations are needed to understand the link between the GNPs inducing an increase in the ROS level and mitochondria dysfunction. An electrostatic interaction between the GNP-coating positive charge and the mitochondria lipid membrane could disrupt its membrane potential, a process known to induce cell oxidative stress. On the other hand, an increase in cytoplasmic oxidative stress could affect the mitochondria. It is interesting to note that the ROS level and the mitochondria potential are two well-known pathways implicated in the induction of cell death, especially by apoptosis [55]. Furthermore, the aforementioned biological dysfunctions are time-dependent, undergoing a partial recovery after a 24-h incubation. We propose that this could explain the difference in radiation enhancement at 6 h compared with 24 h of GNP incubation.

In view of its involvement in a variety of biological pathways, the TrxR system was suggested as an interesting target for clinical applications [56–58]. TrxR is the only known enzyme that catalyzes the reduction of oxidized thioredoxin by coupling with the oxidation of NADPH to NADP$^+$ [59]. Thioredoxin (Trx) is a small protein found in all known organisms that is involved in the activity regulation of other proteins such as Trx peroxidase (which breaks down cytoplasmic H_2O_2 to H_2O) or ribonucleotide peroxidase (which allows DNA synthesis by the ribonucleotide reduction to deoxyribonucleotide) [57,59,60]. In this work, we highlighted TrxR inhibition in cells preincubated with GNPs and demonstrated that a decrease in TrxR activity radiosensitized cells. All together, these results suggest a new biological mechanism of action for the radiosensitization effect of GNPs (Figure 7). Following cellular uptake through a receptor-mediated endocytosis, endosomes containing GNPs fuse with lysosomes. The decrease in pH inside the vesicle could trigger an *in situ* degradation of the GNPs, leading to the release of gold ions [61]. These ions could interact with the TrxR through the formation of an Au-S bond with the thiol active site of the enzyme as demonstrated by various groups [56,62]. This chemical interaction inhibits the TrxR enzyme leading to a disruption in the oxidized–reduced Trx balance. Then, the decrease in the amount of reduced Trx further impacts the Trx peroxidase activity resulting in the accumulation of ROS in the cytoplasm, causing oxidative stress. These radicals could react with biomolecules and organelles such as mitochondria, leading to a mitochondrial depolarization and therefore a decrease in the ATP production. This drop in the energy source of cells could interfere with various biological pathways, especially the DNA damage repair leading to a decrease in the DNA repair process rate observed in this study. Moreover, the extra ROS produced by the interaction between biological matter and ionizing radiation will increase the oxidative stress in a cell with limited detoxification systems to counteract them due to TrxR inhibition. Overall, this new mechanism suggests that GNPs exert their radiosensitizer effect by
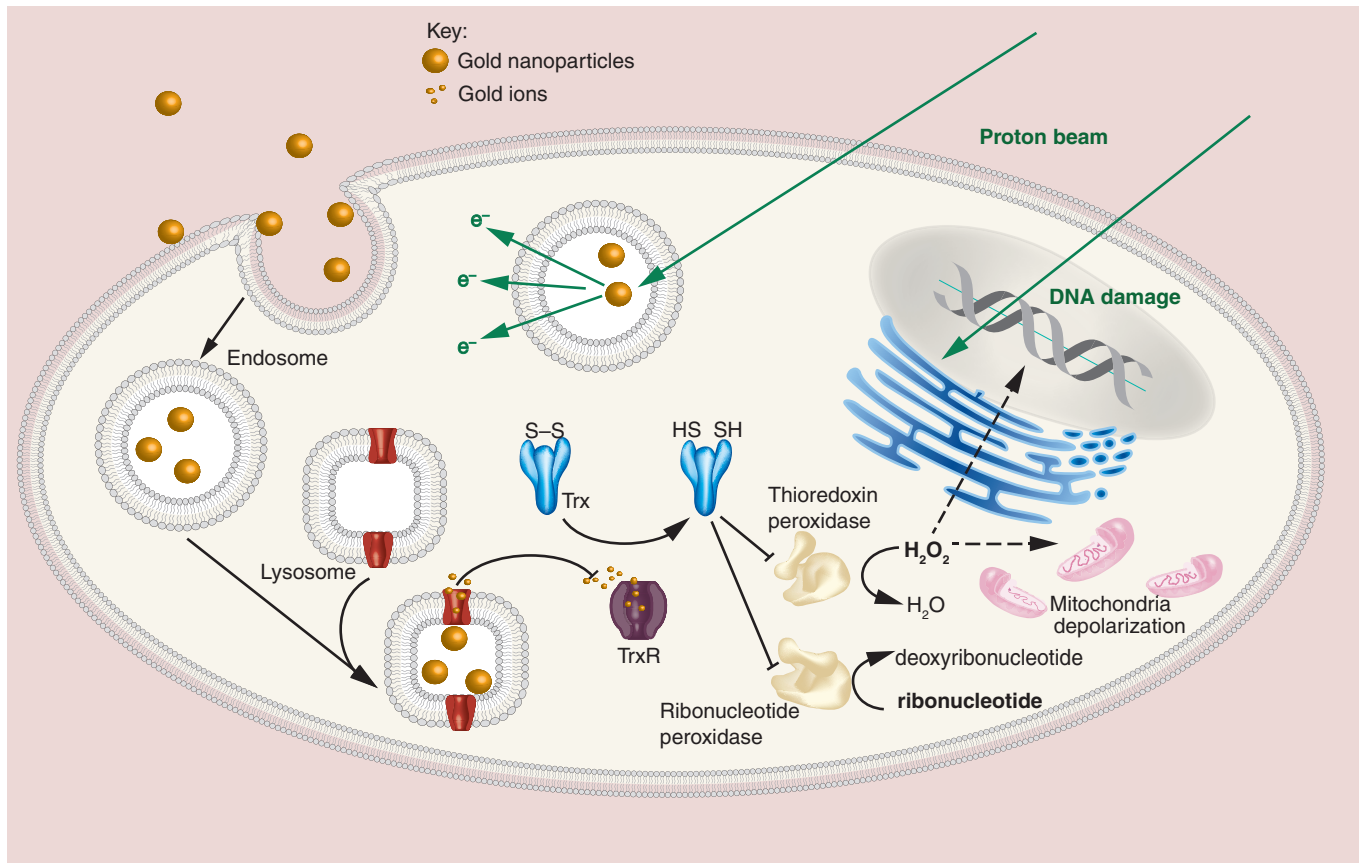
Figure 7. A549 cell exposed to 0.1 Gy of 25 keV/μm proton beam. Following cell uptake through a receptor-mediated endocytosis, endosomes containing GNPs fuse with lysosomes. The decrease in pH inside the vesicle triggers a restricted *in situ* degradation of the GNPs leading to the release of gold ions. An Au-S bond is created between gold ions and the thiol-active site of TrxR, leading to a disruption in the oxidized – reduced Trx balance. Then, the decrease in the amount of reduced Trx further impacts the Trx peroxidase activity resulting in the accumulation of ROS in the cytoplasm generating an oxidative stress. These radicals could react with mitochondria leading to a mitochondrial depolarization and therefore a decrease in the ATP production. This drop in energy source could interfere with various biological pathways, especially DNA damage repair leading to a decrease in the DNA repair process rate. GNP: Gold nanoparticle; ROS: Reactive oxygen species; Trx: Thioredoxin; TrxR: Thioredoxin reductase.

weakening the detoxification systems in the cell before the irradiation rather than via a radioenhancement effect. Recently, protein disulfide isomerase was suspected to be a key mediator of the cellular response to GNPs [21]. The similarity between the enzyme active site and the TrxR one suggests that GNPs could interact with various other thiol-reductase proteins, widely present in oxidative stress response pathways or with antioxidants (such as glutathione).

In recent years, the pharmaceutic industry has tried to find new uses for old already the US FDA-approved drugs. In this context, auranofin [2,3,4,6-tetra-*o*-acetyl-L-thio-β-D-glycopyranosato-*S*-(triethylphosphine)-gold(I)], a TrxR inhibitor used for the treatment of rheumatoid arthritis, has attracted renewed attention as a prospective anticancer agent [63]. Numerous studies have evidenced the ability of auranofin to trigger ROS overproduction and apoptosis in various cancer cell lines [64–66] paving the way to lung cancer [67], leukemia [68] or ovarian cancer [69] clinical trials. In a recent work, Wang *et al*. [66] evidenced that TrxR inhibition greater than 50% could be obtained by incubating 4T1 and EMT6 cell lines with auranofin in a 5–10 μM concentration range. This TrxR inhibition radiosensitized both cell lines to x-ray irradiation. However, they also highlighted that the drug decreased cell viability in a dose-dependent manner with IC_{50} values of 19 and 11 μM for 4T1 and EMT6 cells, respectively. These results demonstrate the toxicity associated to the use of auranofin and bring in light the potential added value of GNPs, for which a powerful TrxR inhibition can be reached without significant cytotoxicity.

Conclusion & future perspective

This work highlights the importance of the nanoparticle–cell interactions to fully understand the radiosensitization mechanism. Indeed, it constitutes the first proof-of-concept that GNP can radiosensitize cells by inhibiting detoxification enzymes. Nevertheless, *in vivo* studies are required to investigate metabolic changes in tumor when GNPs are injected into mice. Besides GNPs, other nanomaterials should be considered and their capacity to inhibit the thiol-reductases protein family (such as TrxR) or antioxidants needs to be assessed for the development of nanotechnologies associated to radiotherapy applications. Mechanistic studies still remain a mandatory step toward the clinical use of nanomaterials as radiosensitizers.

Summary points

- 10 nm amino-PEG functionalized gold nanoparticles (GNPs) were successfully internalized by A549 cells and exerted a marked radiosensitization effect when cells were irradiated with 25 keV/μm protons or 225 kV x-rays.
- We evidenced a mitochondria membrane depolarization and an oxidative stress after a 6-h incubation in the presence of GNPs followed by a recovery at 24-h incubation. These observations are correlated with a more important radiosensitization effect at 6 h of incubation compared with 24 h, demonstrating for the first time that GNP-induced radiosensitivity was modulated overtime.
- We reported a marked inhibition of thioredoxin reductase (TrxR) in cells incubated with GNPs. Moreover, the irradiation of cells invalidated for TrxR evidenced a radiosensitization effect, suggesting that GNPs exert their radiosensitization effect via the inhibition of this enzyme.
- All together, the results suggest that the inhibition of TrxR can lead to an accumulation of reactive oxygen species in the cytoplasm, damaged mitochondria and therefore to a decrease in the ATP production. This drop in the ATP content could decrease the DNA repair rate after irradiation. Moreover, the extra reactive oxygen species produced by interaction between biological matter and ionizing radiation will increase the oxidative stress in cells, which have limited detoxification systems due to TrxR inhibition. Overall, this new mechanism suggests that GNPs exert their radiosensitizer effects by weakening detoxification systems in the cells before irradiation.

Supplementary data

To view the supplementary data that accompany this paper please visit the journal website at: www.futuremedicine.com/doi/full/10.2217/nnm-2018-0171

References

Papers of special note have been highlighted as: ● of interest; ●● of considerable interest

1   Delaney G, Jacob S, Featherstone C, Barton M. The role of radiotherapy in cancer treatment: estimating optimal utilization from a review of evidence-based clinical guidelines. *Cancer* 104(6), 1129–1137 (2005).

2   Wilson RR. Radiological use of fast protons. *Radiology* 47(5), 487–491 (1946).

3   Brown A, Suit H. The centenary of the discovery of the Bragg peak. *Radiother. Oncol.* 73(3), 265–268 (2004).

4   Boisselier E, Astruc D. Gold nanoparticles in nanomedicine: preparations, imaging, diagnostics, therapies and toxicity. *Chem. Soc. Rev.* 38(6), 1759–1782 (2009).

5   Ghosh P, Han G, De M, Kim CK, Rotello VM. Gold nanoparticles in delivery applications. *Adv. Drug Deliv. Rev.* 60(11), 1307–1315 (2008).

6   Mieszawska AJ, Mulder WJ, Fayad ZA, Cormode DP. Multifunctional gold nanoparticles for diagnosis and therapy of disease. *Mol. Pharma.* 10(3), 831–847 (2013).

7   Saha K, Agasti SS, Kim C, Li X, Rotello VM. Gold nanoparticles in chemical and biological sensing. *Chem. Rev.* 112(5), 2739–2779 (2012).

8   Hainfeld JF, Slatkin DN, Smilowitz HM. The use of gold nanoparticles to enhance radiotherapy in mice. *Phys. Med. Biol.* 49(18), N309–N315 (2004).

9   Jeynes JC, Merchant MJ, Spindler A, Wera AC, Kirkby KJ. Investigation of gold nanoparticle radiosensitization mechanisms using a free radical scavenger and protons of different energies. *Phys. Med. Biol.* 59(21), 6431–6443 (2014).

10   Li S, Penninckx S, Karmani L *et al.* LET-dependent radiosensitization effects of gold nanoparticles for proton irradiation. *Nanotechnology* 27(45), 455101 (2016).

11   Li S, Porcel E, Remita H *et al.* Platinum nanoparticles: an exquisite tool to overcome radioresistance. *Cancer Nanotechnol.* 8(1), 4 (2017).

12   Miladi I, Aloy MT, Armandy E *et al.* Combining ultrasmall gadolinium-based nanoparticles with photon irradiation overcomes radioresistance of head and neck squamous cell carcinoma. *Nanomedicine* 11(1), 247–257 (2015).

13   Zhang H, Patel N, Ding S, Xiong J, Wu P. Theranostics for hepatocellular carcinoma with Fe_3O_4@ZnO nanocomposites. *Biomater. Sci.* 4(2), 288–298 (2016).

14   Bhattarai SR, Derry PJ, Aziz K *et al.* Gold nanotriangles: scale up and X-ray radiosensitization effects in mice. *Nanoscale* 9(16), 5085–5093 (2017).

15   Zhang X-D, Luo Z, Chen J *et al.* Ultrasmall glutathione-protected gold nanoclusters as next generation radiotherapy sensitizers with high tumor uptake and high renal clearance. *Sci. Rep.* 5, 8669 (2015).

16   Currell F, Villagomez-Bernabe B. Physical and chemical processes for gold nanoparticles and ionising radiation in medical contexts. In: *Gold Nanoparticles for Physics, Chemistry and Biology.* Scientific W (Ed.). World Scientific, NJ, USA, 509–536 (2017).

17   Miladi I, Alric C, Dufort S *et al.* The *in vivo* radiosensitizing effect of gold nanoparticles based MRI contrast agents. *Small* 10(6), 1116–1124 (2014).

18   Rosa S, Connolly C, Schettino G, Butterworth KT, Prise KM. Biological mechanisms of gold nanoparticle radiosensitization. *Cancer Nanotechnol.* 8(1), (2017).

•   **Review highlighting the potential underlying biological mechanisms in gold nanoparticle radiosensitization.**

19   Rezaee Z, Yadollahpour A, Bayati V, Negad Dehbashi F. Gold nanoparticles and electroporation impose both separate and synergistic radiosensitizing effects in HT-29 tumor cells: an in vitro study. *Int. J. Nanomedicine* 12, 1431–1439 (2017).

20   Arab-Bafrani Z, Saberi A, Tahmasebi Birgani MJ, Shahbazi-Gahrouei D, Abbasian M, Fesharaki M. Gold nanoparticle and mean inactivation dose of human intestinal colon cancer HT-29 cells. *Jundishapur J. Nat. Pharm. Prod.* 10(4), 29153 (2015).

21   Taggart LE, Mcmahon SJ, Butterworth KT, Currell FJ, Schettino G, Prise KM. Protein disulphide isomerase as a target for nanoparticle-mediated sensitisation of cancer cells to radiation. *Nanotechnology* 27(21), 215101 (2016).

22   Taggart LE, Mcmahon SJ, Currell FJ, Prise KM, Butterworth KT. The role of mitochondrial function in gold nanoparticle mediated radiosensitisation. *Cancer Nanotechnol.* 5(1), 5 (2014).

23   Coulter JA, Jain S, Butterworth KT *et al.* Cell type-dependent uptake, localization, and cytotoxicity of 1.9 nm gold nanoparticles. *Int. J. Nanomedicine* 7, 2673–2685 (2012).

24   Jain S, Coulter JA, Hounsell AR *et al.* Cell-specific radiosensitization by gold nanoparticles at megavoltage radiation energies. *Int. J. Radiat. Oncol. Biol. Phys.* 79(2), 531–539 (2011).

25   Polf JC, Bronk LF, Driessen WH, Arap W, Pasqualini R, Gillin M. Enhanced relative biological effectiveness of proton radiotherapy in tumor cells with internalized gold nanoparticles. *Appl. Phys. Lett.* 98(19), 193702 (2011).

26   Butterworth KT, Coulter JA, Jain S *et al.* Evaluation of cytotoxicity and radiation enhancement using 1.9 nm gold particles: potential application for cancer therapy. *Nanotechnology* 21(29), 295101 (2010).

27   Liu Y, Liu X, Jin X *et al.* The dependence of radiation enhancement effect on the concentration of gold nanoparticles exposed to low- and high-LET radiations. *Phys. Med.* 31(3), 210–218 (2015).

28   Huo S, Ma H, Huang K *et al.* Superior penetration and retention behavior of 50 nm gold nanoparticles in tumors. *Cancer Res.* 73(1), 319–330 (2013).

29   Zhang G, Yang Z, Lu W *et al.* Influence of anchoring ligands and particle size on the colloidal stability and in vivo biodistribution of polyethylene glycol-coated gold nanoparticles in tumor-xenografted mice. *Biomaterials* 30(10), 1928–1936 (2009).

30   Zhang XD, Luo Z, Chen J *et al.* Ultrasmall Au10–12 (SG) 10–12 nanomolecules for high tumor specificity and cancer radiotherapy. *Adv. Mater.* 26(26), 4565–4568 (2014).

31   Liang G, Jin X, Zhang S, Xing D. RGD peptide-modified fluorescent gold nanoclusters as highly efficient tumor-targeted radiotherapy sensitizers. *Biomaterials* 144, 95–104 (2017).

32   Guo T. *X-ray Nanochemistry: Concepts and Development.* Springer International Publishing, Cham, Switzerland (2018).

•   **Extensive review of the potential of metallic nanoparticules for cancer therapy.**

33   Oh E, Susumu K, Goswami R, Mattoussi H. One-phase synthesis of water-soluble gold nanoparticles with control over size and surface functionalities. *Langmuir* 26(10), 7604–7613 (2010).

34   Tsai SW, Chen YY, Liaw JW. Compound cellular imaging of laser scanning confocal microscopy by using gold nanoparticles and dyes. *Sensors* 8(4), 2306–2316 (2008).

35   Heuskin AC, Wera AC, Riquier H, Michiels C, Lucas S. Low-dose hypersensitivity and bystander effect are not mutually exclusive in A549 lung carcinoma cells after irradiation with charged particles. *Radiat. Res.* 180(5), 491–498 (2013).

36   Wéra AC, Riquier H, Heuskin AC, Michiels C, Lucas S. *In vitro* irradiation station for broad beam radiobiological experiments. *Nucl. Instrum. Methods Phys. Res.* 269(24), 3120–3124 (2011).

37   Neumaier T, Swenson J, Pham C *et al.* Evidence for formation of DNA repair centers and dose–response nonlinearity in human cells. *Proc. Natl Acad. Sci. USA* 109(2), 443–448 (2012).

38   Toduka Y, Toyooka T, Ibuki Y. Flow cytometric evaluation of nanoparticles using side-scattered light and reactive oxygen species-mediated fluorescence-correlation with genotoxicity. *Environment. Sci. Technol.* 46(14), 7629–7636 (2012).

39   Schultz LB, Chehab NH, Malikzay A, Halazonetis TD. p53 binding protein 1 (53BP1) is an early participant in the cellular response to DNA double-strand breaks. *J. Cell Biol.* 151(7), 1381–1390 (2000).

40   Chithrani BD, Ghazani AA, Chan WC. Determining the size and shape dependence of gold nanoparticle uptake into mammalian cells. *Nano Lett.* 6(4), 662–668 (2006).

41   Hühn D, Kantner K, Geidel C *et al.* Polymer-coated nanoparticles interacting with proteins and cells: focusing on the sign of the net charge. *ACS Nano* 7(4), 3253–3263 (2013).

42   Fogh SE, Andrews DW, Glass J *et al.* Hypofractionated stereotactic radiation therapy: an effective therapy for recurrent high-grade gliomas. *J. Clin. Oncol.* 28(18), 3048–3053 (2010).

43   Timmerman R, Paulus R, Galvin J *et al.* Stereotactic body radiation therapy for inoperable early stage lung cancer. *JAMA* 303(11), 1070–1076 (2010).

44   Hespeels F, Heuskin AC, Scifoni E, Kraemer M, Lucas S. Backscattered electron emission after proton impact on carbon and gold films: experiments and simulations. *Nucl. Instrum. Methods Phys. Res.* 401(Suppl. C), 8–17 (2017).

45   Porcel E, Tillement O, Lux F *et al.* Gadolinium-based nanoparticles to improve the hadrontherapy performances. *Nanomedicine* 10(8), 1601–1608 (2014).

46   Misawa M, Takahashi J. Generation of reactive oxygen species induced by gold nanoparticles under x-ray and UV Irradiations. *Nanomedicine* 7(5), 604–614 (2011).

47   Sicard-Roselli C, Brun E, Gilles M *et al.* A new mechanism for hydroxyl radical production in irradiated nanoparticle solutions. *Small* 10(16), 3338–3346 (2014).

48   Minai L, Yeheskely-Hayon D, Yelin D. High levels of reactive oxygen species in gold nanoparticle-targeted cancer cells following femtosecond pulse irradiation. *Sci. Rep.* 3, 2146 (2013).

49   Heuskin AC, Gallez B, Feron O, Martinive P, Michiels C, Lucas S. Metallic nanoparticles irradiated by low-energy protons for radiation therapy: Are there significant physical effects to enhance the dose delivery? *Med. Phys.* doi:10.1002/mp.12362 (2017) (Epub ahead of print).

50   Sotiropoulos M, Henthorn NT, Warmenhoven JW, Mackay RI, Kirkby KJ, Merchant MJ. Modelling direct DNA damage for gold nanoparticle enhanced proton therapy. *Nanoscale* 9(46), 18413–18422 (2017).

51   Piret JP, Jacques D, Audinot JN *et al.* Copper(II) oxide nanoparticles penetrate into HepG2 cells, exert cytotoxicity via oxidative stress and induce pro-inflammatory response. *Nanoscale* 4(22), 7168–7184 (2012).

52   Wu H, Lin J, Liu P *et al.* Reactive oxygen species acts as executor in radiation enhancement and autophagy inducing by AgNPs. *Biomaterials* 101, 1–9 (2016).

53   Wang Y, Nartiss Y, Steipe B, Mcquibban GA, Kim PK. ROS-induced mitochondrial depolarization initiates PARK2/PARKIN-dependent mitochondrial degradation by autophagy. *Autophagy* 8(10), 1462–1476 (2012).

54   Karatas OF, Sezgin E, Aydin O, Culha M. Interaction of gold nanoparticles with mitochondria. *Colloids Surf. B, Biointerfaces* 71(2), 315–318 (2009).

55   Heiskanen KM, Bhat MB, Wang HW, Ma J, Nieminen AL. Mitochondrial depolarization accompanies cytochrome c release during apoptosis in PC6 cells. *J. Biol. Chem.* 274(9), 5654–5658 (1999).

56   Casini A, Messori L. Molecular mechanisms and proposed targets for selected anticancer gold compounds. *Curr. Topics Med. Chem.* 11(21), 2647–2660 (2011).

57   Saccoccia F, Angelucci F, Boumis G *et al.* Thioredoxin reductase and its inhibitors. *Curr. Protein Peptide Sci.* 15(6), 621–646 (2014).

58   Biaglow JE, Miller RA. The thioredoxin reductase/thioredoxin system: novel redox targets for cancer therapy. *Cancer Biol. Therap.* 4(1), 6–13 (2005).

59   Arner ES, Holmgren A. The thioredoxin system in cancer. *Seminars Cancer Biol.* 16(6), 420–426 (2006).

60   Dunn LL, Buckle AM, Cooke JP, Ng MK. The emerging role of the thioredoxin system in angiogenesis. *Arterioscler. Thromb. Vasc. Biol.* 30(11), 2089–2098 (2010).

61   Sabella S, Carney RP, Brunetti V *et al.* A general mechanism for intracellular toxicity of metal-containing nanoparticles. *Nanoscale* 6(12), 7052–7061 (2014).

●●   **First evidence of ion release from metallic nanoparticle elicited by the acidic conditions of the lysosome.**

62   Cai W, Zhang L, Song Y *et al.* Small molecule inhibitors of mammalian thioredoxin reductase. *Free Radical Biol. Medicine* 52(2), 257–265 (2012).

63   Roder C, Thomson MJ. Auranofin: repurposing an old drug for a golden new age. *Drugs R&D* 15(1), 13–20 (2015).

64   Fiskus W, Saba N, Shen M *et al.* Auranofin induces lethal oxidative and endoplasmic reticulum stress and exerts potent preclinical activity against chronic lymphocytic leukemia. *Cancer Res.* 74(9), 2520–2532 (2014).

65   Zou P, Chen M, Ji J *et al.* Auranofin induces apoptosis by ROS-mediated ER stress and mitochondrial dysfunction and displayed synergistic lethality with piperlongumine in gastric cancer. *Oncotarget* 6(34), 36505–36521 (2015).

66   Wang H, Bouzakoura S, De Mey S *et al.* Auranofin radiosensitizes tumor cells through targeting thioredoxin reductase and resulting overproduction of reactive oxygen species. *Oncotarget* 8(22), 35728–35742 (2017).

67   Sirolimus and auranofin in treating patients with advanced or recurrent non-small cell lung cancer or small cell lung cancer. ClinicalTrials.org

68   Phase I and II study of auranofin in chronic lymphocytic leukemia (CLL). ClinicalTrials.org

69   Auranofin in treating patients with recurrent epithelial ovarian, primary peritoneal, or fallopian tube cancer. ClinicalTrials.org